Bioactive Materials 4 (2019) 346–357

Contents lists available at ScienceDirect

Bioactive Materials

journal homepage: http://www.keaipublishing.com/biomat

Micro/nano-structured TiO_2 surface with dual-functional antibacterial effects for biomedical applications

Xiang Ge[a,b,***], Chengzu Ren[a,**], Yonghui Ding[c,d], Guang Chen[a], Xiong Lu[e], Kefeng Wang[f], Fuzeng Ren[g], Meng Yang[b], Zhuochen Wang[h], Junlan Li[a], Xinxin An[i], Bao Qian[j], Yang Leng[b,*]

[a] Key Laboratory of Mechanism Theory and Equipment Design of Ministry of Education, School of Mechanical Engineering, Tianjin University, Tianjin, 300354, China
[b] Department of Mechanical and Aerospace Engineering, The Hong Kong University of Science and Technology, Clear Water Bay, Kowloon, Hong Kong, China
[c] Center for Advanced Regenerative Engineering, Northwestern University, Evanston, IL, 60208, USA
[d] Department of Biomedical Engineering, Northwestern University, Evanston, IL 60208, USA
[e] Key Lab of Advanced Technologies of Materials, Ministry of Education, School of Materials Science and Engineering, Southwest Jiaotong University, Chengdu, 610031, China
[f] National Engineering Research Center for Biomaterials, Sichuan University, Chengdu, 610064, China
[g] Department of Materials Science and Engineering, Southern University of Science and Technology, Shenzhen, Guangdong, 518055, China
[h] State Key Laboratory of Precision Measuring Technology and Instruments, Tianjin University, Tianjin, 300072, China
[i] School of Humanities, Tianjin Agricultural University, Tianjin, 300384, China
[j] Department of Machine Elements and Engineering Design, University of Kassel, Kassel, 34125, Germany

ARTICLE INFO

Keywords:
Titanium dioxide
Micro/nano-structured surface
Topographical bacteriostatic activity
Photocatalytic bactericidal property
Non-invasive treatment

ABSTRACT

Implant-associated infections are generally difficult to cure owing to the bacterial antibiotic resistance which is attributed to the widespread usage of antibiotics. Given the global threat and increasing influence of antibiotic resistance, there is an urgent demand to explore novel antibacterial strategies other than using antibiotics. Recently, using a certain surface topography to provide a more persistent antibacterial solution attracts more and more attention. However, the clinical application of biomimetic nano-pillar array is not satisfactory, mainly because its antibacterial ability against Gram-positive strain is not good enough. Thus, the pillar array should be equipped with other antibacterial agents to fulfill the bacteriostatic and bactericidal requirements of clinical application. Here, we designed a novel model substrate which was a combination of periodic micro/nano-pillar array and TiO_2 for basically understanding the topographical bacteriostatic effects of periodic micro/nano-pillar array and the photocatalytic bactericidal activity of TiO_2. Such innovation may potentially exert the synergistic effects by integrating the persistent topographical antibacterial activity and the non-invasive X-ray induced photocatalytic antibacterial property of TiO_2 to combat against antibiotic-resistant implant-associated infections. First, to separately verify the topographical antibacterial activity of TiO_2 periodic micro/nano-pillar array, we systematically investigated its effects on bacterial adhesion, growth, proliferation, and viability in the dark without involving the photocatalysis of TiO_2. The pillar array with sub-micron motif size can significantly inhibit the adhesion, growth, and proliferation of *Staphylococcus aureus* (*S. aureus*) and *Escherichia coli* (*E. coli*). Such antibacterial ability is mainly attributed to a spatial confinement size-effect and limited contact area availability generated by the special topography of pillar array. Moreover, the pillar array is not lethal to *S. aureus* and *E. coli* in 24 h. Then, the X-ray induced photocatalytic antibacterial property of TiO_2 periodic micro/nano-pillar array *in vitro* and *in vivo* will be systematically studied in a future work. This study could shed light on the direction of surface topography design for future medical implants to combat against antibiotic-resistant implant-associated infections without using antibiotics.

Peer review under responsibility of KeAi Communications Co., Ltd.

* Corresponding author.
** Corresponding author.
*** Corresponding author. Key Laboratory of Mechanism Theory and Equipment Design of Ministry of Education, School of Mechanical Engineering, Tianjin University, Tianjin, 300354, China.
E-mail addresses: gexiang.hkust@gmail.com (X. Ge), renchz@tju.edu.cn (C. Ren), meleng@ust.hk (Y. Leng).

https://doi.org/10.1016/j.bioactmat.2019.10.006
Received 7 August 2019; Received in revised form 10 October 2019; Accepted 17 October 2019
Available online 01 November 2019

1. Introduction

Medical implants have revolutionized modern medicine, but they also involve a higher risk of implant-associated infection that is a severe and frequent complication related to biomaterial applications [1–3]. In the USA, the implant-associated infections account for 25.6% of all healthcare-associated infections [4]. Notably, the implant-associated infections are generally difficult to cure owing to the bacterial antibiotic resistance [3] which is attributed to the widespread usage of antibiotics [5,6]. Many eventual failures of medical implants are caused by the bacterial infection at healing sites [7–11]. Currently, antibiotic-resistant infections result in 700,000 deaths per year all over the world [5]. If there is still no effective solution to combat against the antibiotic resistance, the number of global victims will rise dramatically to 10,000,000 per year by the middle of the 21st century [5].

Given the global threat and increasing influence of antibiotic resistance, there is an urgent demand to explore novel antibacterial strategies other than using antibiotics [12–20]. Recently, using a certain surface topography to provide a more persistent antibacterial solution attracts more and more attention [5,21–26]. Traditionally, researchers focused on the bacterial responses to the surfaces with different roughness values (R_a), but the conclusions were contradictory [27–31], because the surfaces with identical R_a values could possess totally different surface topographies and identical randomly textured surfaces can hardly be reproduced [32]. Alternatively, researchers turned to devote efforts in studying the bacterial responses on reproducible regular patterned surfaces which were inspired by natural antifouling surfaces [33]. In our previous studies, we demonstrated that Si periodic pillar arrays with sub-micron motif sizes could significantly inhibit bacterial adhesion, proliferation, and colonization by a spatial confinement size-effect [34,35]. Our findings suggested that nano-pillar array might be the optimal topography design against bacteria, which was coincident with the design of nature for the bactericidal topographies on the surface of cicada wing [36–41], dragonfly wing [38,41,42], and gecko skin [43]. The findings [34] were reported even before the first announcement of the natural bactericidal topography on the surface of cicada wing [36].

However, the clinical application of biomimetic nano-pillar array is not satisfactory [41], mainly because its antibacterial ability against Gram-positive strain including *Staphylococcus aureus* (*S. aureus*) is not good enough [37]. Since *S. aureus* usually causes implant-associated infections [3,44], the biomimetic nano-pillar array should be equipped with other antibacterial agents to fulfill the bacteriostatic and bactericidal requirements of clinical application. Recently, Ye et al. [41] combined a nano-pillar array and ZnO nanoslices to prepare a cicada & catkin inspired structure that was demonstrated to simultaneously have ideal biocompatibility, better bacterial anti-adhesive property, broader antibacterial range, and long-lasting antibacterial activity. ZnO-based nanomaterials possess high antibacterial activity against both Gram-positive and -negative bacterial strains [45–48], which has been mainly attributed to Zn^{2+} ions release, bacterial cell membrane damage, and photocatalytic generation of reactive oxygen species (ROS) [49,50].

Similar to ZnO, TiO_2 is another popular biocompatible and bioactive biomaterial [51–54] with photocatalytic antibacterial activity which has been ascribed to the generation of ROS that can oxidize organic materials up to complete mineralization [55,56]. Briefly, the organic material oxidization affects the bacterial membrane permeability first (Scheme 1a and 1b), then gradually damages all cell wall layers to make the bacteria leak small molecules and ions (like K^+) (Scheme 1c) followed by higher molecular weight components (e.g., RNA and protein) (Scheme 1d) [56]. Eventually, the degradation of bacterial internal components occurs (Scheme 1e) followed by complete mineralization (Scheme 1f) [56]. UV induced photocatalysis on TiO_2 is well known [56], while the X-ray induced photocatalytic activity of TiO_2 has attracted much more attention for biomedical applications since it has a prominent characteristic that a non-invasive treatment can be achieved by adjusting the X-ray penetration depth through the human body [57]. This implies the X-ray irradiation may be used to intentionally trigger the photocatalysis of TiO_2 *in vivo* to kill the bacteria near or on the TiO_2 surface of a medical implant, which could inhibit the implant-associated biofilm formation or eliminate the already-formed biofilm without surgical or invasive treatments in a controllable manner.

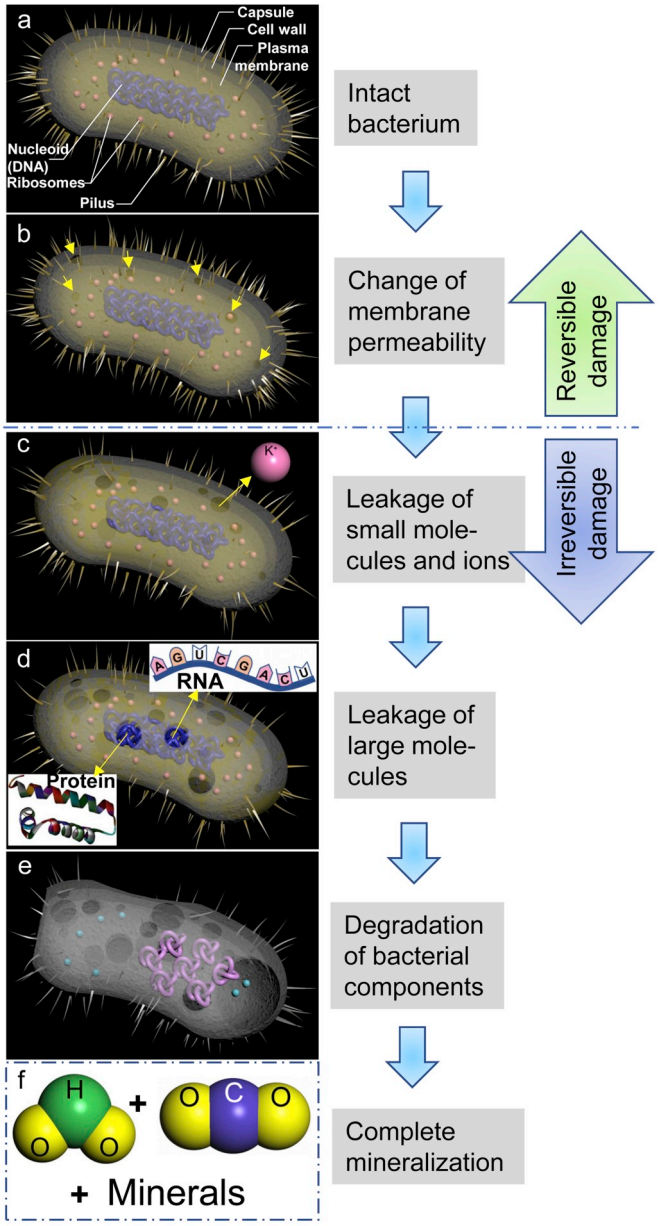

Scheme 1. Schematic illustration for the photocatalytic bactericidal process of a bacterium on TiO_2 surface. (a) An intact bacterium; (b) Bacterial membrane permeability will be affected by an organic material oxidization effect generated from the TiO_2 photocatalysis, but this permeability change is reversible. The arrows indicate the sites where the permeability has been changed; (c) All cell wall layers will be further destroyed, which will make the bacterium leak small molecules and ions (like K^+). Bacterial damage will be irreversible from this stage; (d) Leakage of higher molecular weight components such as RNA and protein; (e) Degradation of bacterial internal components such as nucleoid; (f) Finally, the bacterium will be completely mineralized to H_2O, CO_2, and minerals.

Here, we aimed to design a novel model substrate which was a combination of periodic micro/nano-pillar array and TiO_2 for basically understanding the topographical bacteriostatic effects of periodic micro/nano-pillar array and the photocatalytic bactericidal activity of

TiO_2. Such innovation may potentially exert the synergistic effects by integrating the persistent topographical antibacterial activity and the non-invasive X-ray induced photocatalytic antibacterial property of TiO_2 to combat against antibiotic-resistant implant-associated infections. A high-throughput screening idea was introduced to fabricate one flat area as control and nine patterned areas (motif size 0.6 μm–20 μm) on a single chip for efficiently discovering which size of TiO_2 periodic pillar array possessed higher antibacterial activity. Sphere-shaped *S. aureus* and rod-shaped *Escherichia coli* (*E. coli*) were employed in this work since they are common pathogens for medical implant infections [3,44] and they have distinct morphologies. First, to separately verify the topographical antibacterial activity of TiO_2 periodic micro/nano-pillar array, we systematically investigated its effects on bacterial adhesion, growth, proliferation, and viability in the dark without involving the photocatalysis of TiO_2. Then, the X-ray induced photocatalytic antibacterial property of TiO_2 periodic micro/nano-pillar array *in vitro* and *in vivo* will be systematically studied in a future work.

2. Materials and methods

2.1. Preparation of TiO_2 periodic micro/nano-pillar arrays

2.1.1. Photomask design

A photomask design plays a vital role in the photolithography, since the final geometric shape of the micro/nano-scale topography is directly determined by the photomask design which should be placed at the very beginning in the micro/nano-scale topography fabrication process. In this study, we designed to locate one flat area and nine patterned areas on a single Si chip. Every two areas were insulated by a 4-μm-wide fence. As shown in Fig. S1, the pillar array motif size was defined as below:

pillar array motif size = pillar width (W) = pillar length (L) = spacing (S).

There were nine different motif sizes corresponding to nine patterned areas (Fig. S1). Since some motif sizes were shorter than 1 μm, a high-resolution mask aligner (ASML 5000 Stepper, Resolution = 0.5 μm, Reduction ratio = 5:1) was used for photolithography in this study. The design of stepper photomask is schematically shown in Fig. S1. Owing to the reduction ratio (5:1) of the stepper, the original dimension of the pattern on the stepper photomask should be designed 5 times longer than the actual dimension of the motif.

2.1.2. Thermal SiO_2 growth

A SiO_2 layer which works as a mask when etches the Si substrate is needed to grow on the Si substrate surface before photolithography (Fig. 1a). In this step, the SiO_2 layer was generated by Si thermal oxidation other than SiO_2 deposition. A SiO_2 layer with a thickness around 100 nm was obtained by a wet oxidation method using a diffusion furnace (ASM LB 45).

2.1.3. Photolithography

The photolithography consists of 8 sub-steps which are hexamethyldisilazane (HMDS) prime, spinning photoresist (Fig. 1a), soft baking, UV exposure (Fig. 1b), postexposure baking, development (Fig. 1b), hard baking, and de-scumming. All these sub-steps can be completed within a wafer track (SVG WaferTrack) automatically except for the UV exposure which should be conducted using the high-resolution mask aligner (ASML 5000 Stepper). The details of the 8 sub-steps are described in the **Supplementary Data**.

2.1.4. SiO_2 layer etching

The pattern was transferred from the photoresist layer to the SiO_2 layer (Fig. 1c) using an advanced oxide etching (AOE) machine (STS AOE Etcher, Surface Technology Systems, Coventry, UK). Since the plasma reactant has a much higher reaction rate with SiO_2 than with the photoresist, the SiO_2 layer covered by the photoresist pattern will be retained, while other uncovered regions of the SiO_2 layer will be etched by the plasma etchant. Here, the wafers were etched for 1 min to make sure that the uncovered SiO_2 layer (~100 nm thick) could be removed

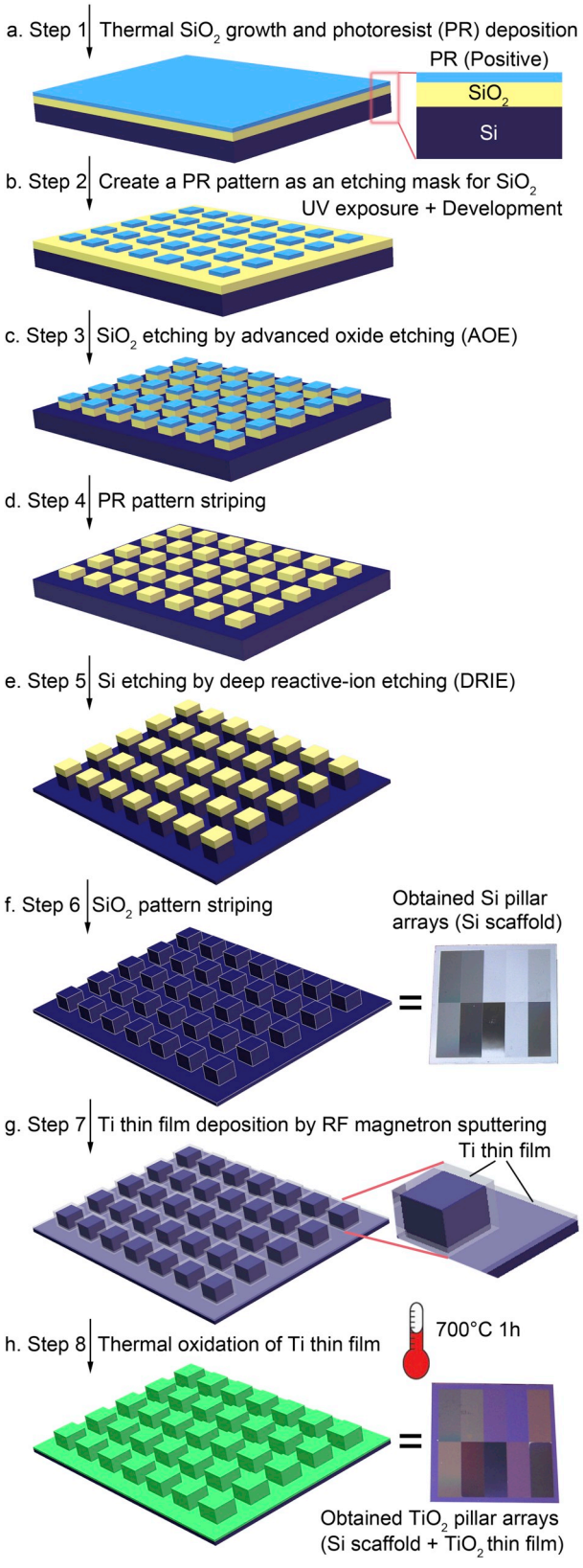

Fig. 1. Schematic illustration for the preparation processes of Si pillar arrays (Si scaffold) and TiO_2 pillar arrays (Si scaffold + TiO_2 thin film).

completely, since the SiO_2 etching rate was around 200 nm/min in the AOE machine.

2.1.5. Photoresist pattern striping

So far, the photoresist pattern had finished its mission as a mask during the SiO_2 layer etching and should be removed (Fig. 1d). Firstly, the photoresist pattern on the Si wafer was dry stripped for 20 min in a photoresist asher (PS210 Photo Resist Asher) after the step of SiO_2 layer etching. Secondly, the photoresist pattern on the Si wafer was wet stripped for 10 min in a $H_2SO_4 + H_2O_2$ bath at 120 °C to further remove any possible remaining photoresist.

2.1.6. Si substrate etching

We employed a deep reactive-ion etching (DRIE) machine (STS ICP DRIE Silicon Etcher) to etch the Si substrate for transferring the pattern from the SiO_2 layer to the Si substrate (Fig. 1e), which was a crucial step in the whole micro/nano-scale topography fabrication process since it directly and finally determined the geometric dimensions of the micro/nano-scale topography on the Si wafer. We used an etching program of which Si etching rate was around 0.143 μm/cycle to etch the Si wafer for 21 cycles aiming at obtaining a final etching depth of around 3 μm.

2.1.7. SiO_2 pattern striping

We immersed the Si wafers into a buffered oxide etching (BOE) solution for 5 min to thoroughly remove the SiO_2 pattern which had finished its mission as a mask during the Si substrate etching. So far, the Si wafers with well-defined geometric Si periodic micro/nano-pillar arrays (Si scaffold) had been obtained (Fig. 1f).

2.1.8. Ti thin film deposition and thermal oxidation

The experimental procedure was conducted according to that in our previous study [58]. Briefly, a RF magnetron sputtering system (Model Explorer 14, Denton Vacuum, Moorestown, NJ, USA) equipped with a target of pure titanium disk (purity = 99.99%) was employed to deposit a pure titanium thin film onto the Si scaffold (Fig. 1g) [58]. The thin film deposition was conducted under an argon gas pressure of 5×10^{-3} Torr at a constant RF power of 100 W at 25 °C for 300 s [58]. Then, the thin film was transformed from pure titanium to TiO_2 by a thermal oxidation at 700 °C with air flow for 1 h (Fig. 1h) [58].

2.2. Characterization of TiO_2 periodic micro/nano-pillar arrays

The morphologies of samples were examined using a field emission scanning electron microscope (FESEM; JSM-6700F, JEOL, Japan). The samples were pasted onto copper stubs using silver glue and double-sided carbon tapes [35,59,60] and coated with a gold thin film. To further decrease the surface charging effect during SEM observation, a low accelerating voltage (5 kV) was employed in this work [61–64].

Surface chemical compositions of samples were analyzed by an X-ray photoelectron spectrometer (XPS; Axis Ultra DLD, Kratos, Japan). The broad range XPS spectra were obtained with an Al K_α excitation source ($h\upsilon$ = 1486.6 eV) and a take-off angle of 90° at a passing energy of 160 eV. The high-resolution spectra of the Ti 2p region were obtained with a passing energy of 40 eV.

An X-ray diffractometer (X'Pert PRO, PANalytical, Netherlands) operating at 40 mA and 40 kV was employed to determine the crystal structure of the thermally oxidized thin film by a thin-film X-ray diffraction (TF-XRD) method [58]. The diffraction patterns were collected using Cu-K_α radiation (wavelength = 1.54056 Å) "in a 2θ range of 20°–80° with a step size of 0.05° and a count time of 2.5 s" [58].

The water contact angles (WCA) of samples were measured by a sessile drop method using a contact angle instrument (DIGIDROP, GBX, France). A motorized-syringe was employed to gently lay a droplet (4 μL) of deionized (DI) water onto a sample surface at room temperature. The instrument recorded the WCAs immediately after laying the droplet onto the sample surface within 30 s. Five measurements of sample WCAs were conducted and the average value corresponding to each sample was presented.

2.3. Bacterial experiments

2.3.1. Bacterial strain culture

As common pathogens for medical implant infections [3,44], *S. aureus* ATCC 25923 (sphere-shaped, Gram-positive) and *E. coli* JM109 (rod-shaped, Gram-negative) were involved in this study. The components of agar and liquid Luria-Bertani (LB) medium which were used as the culture media for both *S. aureus* and *E. coli* are listed in Table S1. The experimental procedure was conducted according to that in our previous study [35]. Briefly, "frozen *S. aureus* or *E. coli* strain was streaked on an agar plate and incubated at 37 °C for a minimum of 12 h" [35]. An aseptic micropipette tip was used to scrape off an as-prepared bacterial colony on the agar plate. Then, the micropipette tip was put into a test tube filled with LB liquid medium. The test tube was incubated in an orbital shaker at 37 °C for one incubation cycle which was determined by bacterial growth curves. Using the bacteria which have entered the exponential phase of growth can ensure the bacteria stay in the same situation for following assays. After incubation, the turbidity (OD_{600}) of the bacterial suspension in the test tube was measured using a turbidimeter (eppendorf BioPhotometer, Eppendorf AG, Hamburg, Germany). The initial bacterial colony forming unit (CFU) density of the bacterial suspension can be calculated via multiplying the OD_{600} value by 10^9 CFU/mL. Finally, according to the pre-test result, the bacterial suspension was diluted to demanded concentrations for different assays with LB liquid medium based on the initial CFU density.

2.3.2. Bacterial adhesion assay

The *S. aureus* or *E. coli* suspension with a CFU density of 7×10^8 CFU/mL was employed. Prior to use, the samples of TiO_2 periodic micro/nano-pillar arrays were "sterilized by steam autoclaving in a high-pressure steam sterilization pot at 121 °C for 20 min" [35]. Then, the samples were immersed into the bacterial suspension and incubated in the dark at 37 °C for 30 min. Before staining, the samples were "gently rinsed with a HEPES Buffered Saline Solution (HBSS)" (Table S2) [35]. All experiments were repeated in triplicate.

2.3.3. Bacterial growth and proliferation assay

The *S. aureus* or *E. coli* suspension with a CFU density of 1×10^5 CFU/mL was employed. Prior to use, the samples of TiO_2 periodic micro/nano-pillar arrays were "sterilized by steam autoclaving in a high-pressure steam sterilization pot at 121 °C for 20 min" [35]. Then, the samples were immersed into the bacterial suspension and incubated in the dark at 37 °C for 12 h and 24 h. Before staining, the samples were gently rinsed with the HBSS [35]. All experiments were repeated in triplicate.

2.4. Bacterial characterization

2.4.1. LIVE/DEAD staining

The experimental procedure was conducted according to that in our previous study [35]. Briefly, a LIVE/DEAD® *Bac*Light™ Bacterial Viability Kit (L7012) was employed to stain the adhered and colonized bacteria on the TiO_2 periodic micro/nano-pillar arrays. The kit contains SYTO® 9 and propidium iodide which are two kinds of nucleic acid stains. "After being cultured for a certain period of time, a chip with the bacteria was gently rinsed by the HBSS, and then incubated with a 0.5 μL: 0.5 μL: 1 mL mixture of SYTO® 9, propidium iodide, and HBSS for 20 min at room temperature in the dark" [35]. Before the following characterizations, the chip was "gently rinsed in HBSS and DI water in sequence and dried in the air at room temperature" [35]. Live bacteria appear green while dead bacteria appear red under a fluorescence microscope.

2.4.2. Confocal laser scanning microscope (CLSM) observation and statistics

The experimental procedure was conducted according to that in our previous study [35]. Briefly, the dried chips were observed under a CLSM (LSM7 DUO (710 + LIVE), Carl Zeiss MicroImaging GmbH, Germany). "The SYTO® 9 green was excited by a 489 nm laser and the emission spectrum from 510 nm to 540 nm was collected in CLSM. The propidium iodide red was excited by a 561 nm laser and the emission spectrum from 620 nm to 650 nm was collected" [35]. Three random regions corresponding to each of the ten areas on the chip were taken pictures under the CLSM using a 3D imaging mode. Each CLSM image showed a view field of 848.53 × 848.53 μm^2 by employing a ×10 objective lens. A software named ImageJ (version 1.43u, National Institutes of Health, USA) was employed to count the bacterial occupied area of each CLSM image. The ratio of the bacterial occupied area out of the whole examined area in each CLSM image was normalized by dividing the average ratio corresponding to TiO_2_Flat (control), and then the results were expressed in percentages which represented the antibacterial ability of different areas on the chip.

2.4.3. SEM observation

The experimental procedure was conducted according to that in our previous study [35]. Briefly, the detailed morphologies of bacteria on the TiO_2 periodic micro/nano-pillar arrays and the TiO_2 flat area were observed using the FESEM (JSM-6700F, JEOL, Japan). "After the CLSM examinations, samples were fixed in a solution (pH = 7.4) mixed with glutaraldehyde ($C_5H_8O_2$, 2.5 wt%) and sodium cacodylate buffer ($Na(CH_3)_2AsO_2{\cdot}3H_2O$, 0.1 M) at 4 °C for 2 h [65,66], dehydrated in an ethanol series (30%, 50%, 70%, 80%, 90%, 100%, and 100%; each step for 5 min), dried using a critical point dryer (Model CPD-2, Pelco), coated with a thin layer of gold, and then observed by the SEM" [35].

2.5. Statistical analysis

All statistical data were expressed as mean ± standard deviation (SD) or standard error of the mean (SEM), which was clearly indicated in relevant figure captions. Significant differences ($p \leq 0.05$) among the groups were detected by a One-way analysis of variance (ANOVA) followed by a Student's t-test. Notably, there was an independent Student's t-test between TiO_{2PA}_0.6 μm and each of the other nine areas on the chip for each set of CLSM observation statistical results.

3. Results

3.1. Characterization results of TiO_2 periodic micro/nano-pillar arrays

The TiO_2 periodic micro/nano-pillar arrays were prepared by a process of Si wafer photolithography plus a RF magnetron sputtering followed by a thermal oxidation, as illustrated in Fig. 1. Firstly, we introduced a high-throughput screening idea to design and fabricate one flat area as control and nine patterned areas on a single Si chip (size = 10 × 10 mm) (Fig. 2a), which ensured that the ten areas could be cultured in the same environment and ten groups of data could be obtained simultaneously after the following bacterial experiments [35]. Thus, the experimental efficiency could be increased by 10 times. Furthermore, every two areas were insulated by a 4-μm-wide and 3-μm-high fence (Fig. 2b) to avoid potential interferences between every two areas in following bacterial experiments [35]. On every patterned area, the pillar width and length were equal to the spacing between two pillars, and the heights of all pillars were 3 μm (Fig. 2b). The nine patterned areas were named with their pillar array motif size as Si_{PA}_20 μm, Si_{PA}_10 μm, Si_{PA}_5 μm, Si_{PA}_2 μm, Si_{PA}_1.4 μm, Si_{PA}_1.2 μm, Si_{PA}_1.0 μm, Si_{PA}_0.8 μm, and Si_{PA}_0.6 μm (Fig. 2c). The flat area was named as Si_Flat (Fig. 2c). Moreover, the location arrangement of the ten areas on a chip was random (Fig. 2a), not according to the pillar array motif size order to avoid potential edge/central effects which might interfere the results obtained from the following bacterial experiments [35]. So far, a Si scaffold had been successfully obtained.

After the RF magnetic sputtering and the thermal oxidation, the chip color changed as shown in Fig. 3a and b, which was an indirect evidence of a thin film formation on the Si scaffold. Fig. 3c shows the morphology of flat Si substrate under a magnification of ×50,000. While after the Ti thin film deposition and the thermal oxidation, it could be seen under the same magnification (× 50,000) that a continuous and dense thin film with small and homogenous size of grains was formed on the flat Si substrate (Fig. 3d). In addition, when comparing morphologies before (Fig. 3e, Fig. S2a, and Fig. S2c) and after (Fig. 3f, Fig. S2b, and Fig. S2d) the Ti thin film deposition and the thermal oxidation, we could find that a thin film with the identical morphology shown in Fig. 3d also formed on the side-wall of the pillar (Fig. 3f), the top of the pillar (Fig. S2b), and the surface of the substrate (Fig. S2d). All these SEM observations provided direct evidences to demonstrate that a conformal thin film was successfully formed on the whole Si pillar array. Since the thin film thickness was only about 52 nm as shown in a cross-section view (Fig. 3g), the topography of the Si scaffold (Fig. 2c) was maintained after the thin film formation.

There was no obvious difference between the broad range XPS spectra of the thin film coated pillar array and the thin film coated flat surface (Fig. 3h). The broad range XPS spectra (Fig. 3h) indicate that the thin film contains the components of Ti and O together with C which is a common surface contamination element. Moreover, the high-resolution XPS spectra corresponding to Ti 2p (Fig. S3) can help to better understand the Ti chemical state. Similarly, there was no obvious difference between the high-resolution XPS spectra of the thin film coated pillar array and the thin film coated flat surface either (Fig. S3). There are two typical electron binding energies of Ti which are 453.6–454.2 eV (oxidation state 0, Ti metal) and 458.8–459.2 eV (oxidation state +IV, TiO_2). The high-resolution XPS spectra corresponding to Ti 2p (Fig. S3) show that the binding energy for Ti 2p peak is at ~458.8 eV, which indicates that all Ti components are Ti^{4+} and Ti^0 do not exist in the thin film. These results confirmed that the sputtered Ti thin film had been completely transformed to TiO_2 by the thermal oxidation.

Notably, both the thin film coated pillar array and the thin film coated flat surface did not exhibit any obvious difference in their XRD diffraction patterns (Fig. 3i). Typical TF-XRD patterns (Fig. 3i) confirm that the crystalline phase of the TiO_2 thin film covering the Si scaffold is rutile. The diffraction patterns (Fig. 3i) do not show any peak of Ti, which double confirms that the thermal oxidation have completely transformed the deposited Ti thin film to TiO_2. In addition, it is reasonable that the Si signal from the substrate shows in the diffraction patterns (Fig. 3i), because the TF-XRD can obtain signals from the bulk material ~1 μm away from the material top surface while the TiO_2 thin film thickness was only about 52 nm as mentioned above.

Finally, well-defined TiO_2 periodic micro/nano-pillar arrays were obtained. Similar to the naming rule of Si scaffold, the ten areas were named as TiO_{2PA}_20 μm, TiO_{2PA}_10 μm, TiO_{2PA}_5 μm, TiO_{2PA}_2 μm, TiO_{2PA}_1.4 μm, TiO_{2PA}_1.2 μm, TiO_{2PA}_1.0 μm, TiO_{2PA}_0.8 μm, TiO_{2PA}_0.6 μm, and TiO_2_Flat.

The results of WCA measurement revealed a significant influence of pillar array motif size on the wettability of patterned TiO_2 surface. As shown in Fig. 3j, the WCAs monotonically reduce from 52.3° to 16.1° with decreasing the pillar array motif size from 20 μm to 0.6 μm. The WCA of TiO_2_Flat was 56.4° (Fig. 3j) which was slightly higher than that of TiO_{2PA}_20 μm. Therefore, all the ten areas were hydrophilic since their WCAs were all smaller than 90°, which indicated that the surface energies (γ) of all the ten areas were relatively high.

3.2. Bacterial adhesion

3.2.1. S. aureus_cultured for 30 min

The experimental results of *S. aureus* adhesion exhibited an evident

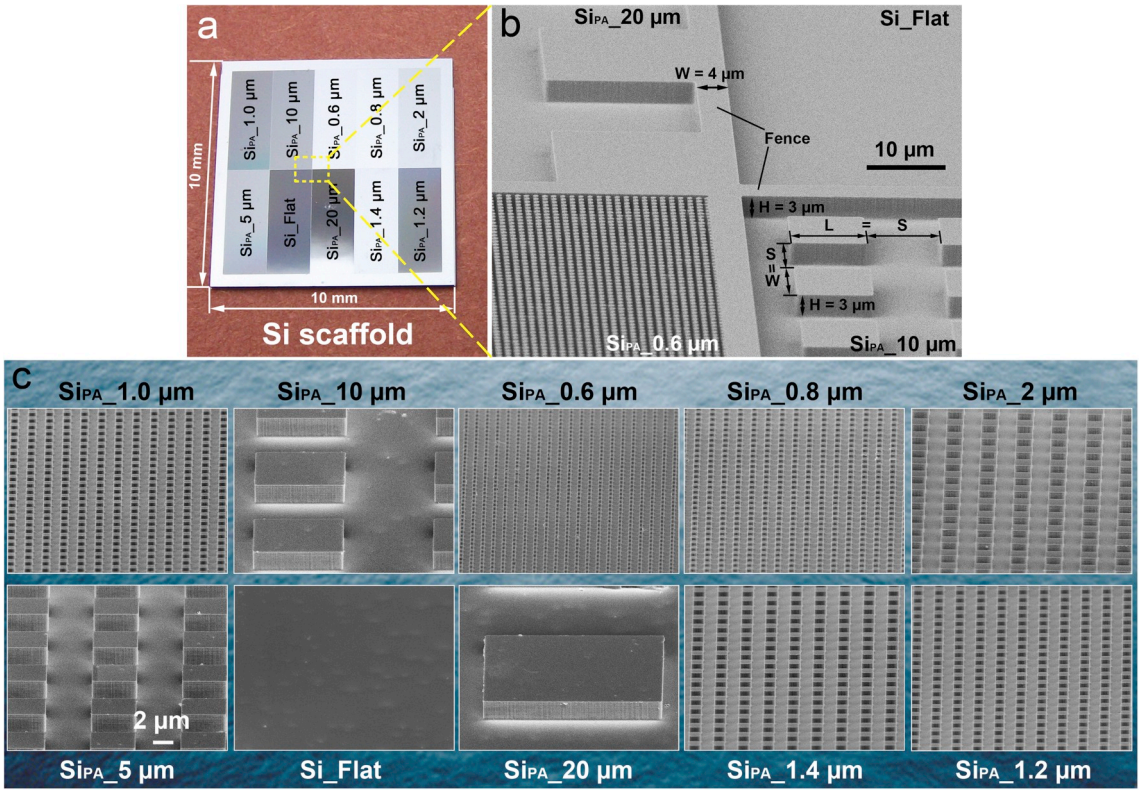

Fig. 2. (a) A single chip of Si scaffold which consists of ten areas including one flat area and nine patterned areas; (b) Every two areas are insulated by a fence of which width is 4 μm and height is the same as that of pillar (3 μm). Pillar array motif size = pillar width (W) = pillar length (L) = spacing (S) between two pillars; (c) SEM angular views of each area.

correlation with the motif size of TiO_2 periodic micro/nano-pillar array. CLSM images (Fig. 4a) depict an obvious difference in *S. aureus* occupied areas corresponding to different patterned areas with distinct pillar array motif sizes, as illustrated by a sharp boundary between every two patterned areas. Qualitatively, the CLSM images clearly indicate that the smaller pillar array motif size such as 0.6 μm results in less bacterial adhesion. However, the TiO_2 periodic micro/nano-pillar array with larger motif size and the flat surface seem favorable for *S. aureus* adhesion. Quantitative statistical analysis (Fig. 4b) of the CLSM images confirms that the normalized bacterial occupied area percentage first increases with decreasing the pillar array motif size and then decreases with further decreasing the pillar array motif size down to the sub-micron level. Comparing to the TiO_2 flat surface, the bacterial adhesion decreases dramatically if the pillar array motif size reduces down to 0.6 μm (only 38% of the bacterial occupied area on TiO_2_Flat, as shown in Fig. 4b), while TiO_{2PA}_1.4 μm has the maximal value of normalized bacteria occupied area percentage (131% of the bacterial occupied area on TiO_2_Flat, as shown in Fig. 4b).

3.2.2. *E. coli* cultured for 30 min

The experimental results of *E. coli* adhesion also exhibited an evident correlation with the motif size of TiO_2 periodic micro/nano-pillar array, though *E. coli* possesses a different shape (rod) other than sphere. Qualitatively, CLSM images (Fig. 4c) intuitively show an obvious difference in *E. coli* densities on different patterned areas with distinct pillar array motif sizes. Similar to the *S. aureus* case, quantitative statistical analysis (Fig. 4d) of the CLSM images also shows a non-monotonic trend of bacterial adhesion with decreasing the pillar array motif size. The trend indicates that the normalized bacterial occupied area percentage first increases with decreasing the pillar array motif size, reaches the maximum (128% of the bacterial occupied area on TiO_2_Flat, as shown in Fig. 4d) when the pillar array motif size equals 5 μm, and then decreases with further decreasing the pillar array motif size down to the sub-micron level. In particular, the TiO_{2PA}_0.6 μm has the most obvious bacterial anti-adhesive effect since it exhibits only 27% of the bacterial occupied area on TiO_2_Flat (Fig. 4d).

3.3. Bacterial growth and proliferation

3.3.1. *S. aureus* cultured for 12 h and 24 h

The experimental results (Fig. 5a and b) of *S. aureus* cultured for 12 h reveal an approximately monotonic decreasing tendency that the normalized bacterial occupied area percentage reduces with decreasing the pillar array motif size. Consistently, the TiO_{2PA}_0.6 μm also has the least bacterial occupied area which is only 12% of that on TiO_2_Flat (Fig. 5b). Nevertheless, the experimental results (Fig. 6a and b) of *S. aureus* cultured for 24 h exhibit a non-monotonic trend of bacterial adhesion with decreasing the pillar array motif size. The trend indicates that the normalized bacterial occupied area percentage first slightly increases with decreasing the pillar array motif size, reaches the maximum (118% of the bacterial occupied area on TiO_2_Flat, as shown in Fig. 6b) when the pillar array motif size equals 2 μm, and then decreases with further decreasing the pillar array motif size down to the sub-micron level. Notably, the TiO_{2PA}_0.6 μm also has the most obvious effect on inhibiting the bacterial proliferation and colonization since it exhibits only 40% of the bacterial occupied area on TiO_2_Flat (Fig. 6b).

3.3.2. *E. coli* cultured for 12 h and 24 h

The results of bacterial growth and proliferation assay reveal an evident pillar array motif size dependent effect on *E. coli* occupied area evidenced by the CLSM images (Fig. 5c cultured for 12 h, and Fig. 6c cultured for 24 h, respectively). Quantitative analysis shown in Fig. 5d (cultured for 12 h) and Fig. 6d (cultured for 24 h) indicates similar trends which first slightly increase and then decrease with decreasing the pillar array motif size. The TiO_2 periodic micro/nano-pillar array shows an obvious effect on inhibiting *E. coli* proliferation and

colonization compared to the TiO_2 flat surface when the pillar array motif size reaches the sub-micron level. Again, the TiO_{2PA}_0.6 μm exhibits the most excellent effect on decreasing *E. coli* population no matter the culture time is 12 h (only 22% of the bacterial occupied area on TiO_2_Flat, as shown in Fig. 5d) or 24 h (only 30% of the bacterial occupied area on TiO_2_Flat, as shown in Fig. 6d).

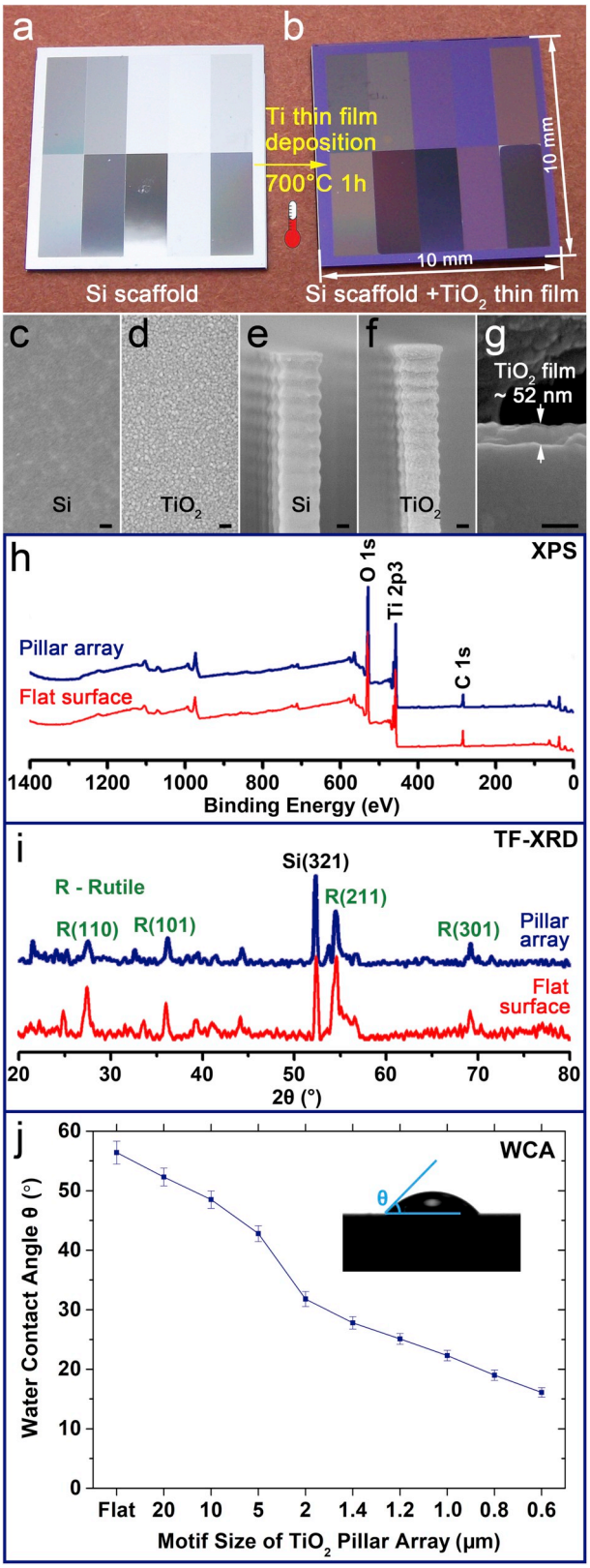

Fig. 3. (a) Si scaffold with ten areas including one flat area and nine patterned areas; (b) Si scaffold coated with a TiO_2 thin film; (c) Morphology of a flat Si substrate (× 50,000, scale bar = 100 nm); (d) Morphology of a TiO_2 thin film on a flat Si substrate (× 50,000, scale bar = 100 nm); (e) Morphology of the side-wall of a Si pillar (× 50,000, scale bar = 100 nm); (f) Morphology of the side-wall of a Si pillar coated with a TiO_2 thin film (× 50,000, scale bar = 100 nm); (g) Cross-section view of a TiO_2 thin film shows that the film thickness is around 52 nm (× 150,000, scale bar = 100 nm); (h) XPS spectra indicate that the thin film (either on the pillar array or on the flat surface) contains the components of Ti and O; (i) TF-XRD patterns confirm that the crystalline phase of the thin film (either on the pillar array or on the flat surface) is rutile; (j) WCAs of one flat and nine patterned TiO_2 areas. Error bar = SD. Inset: illustrating the measuring method of WCA which is smaller than 90°.

3.4. Bacterial viability

In this study, the CLSM images corresponding to TiO_{2PA}_2 μm cultured for 24 h was used as an example for demonstration, since the same conclusion could be drawn from the results of the other nine areas. As depicted in Fig. S4a, there is no red bacteria shown in this merged CLSM image, which suggests that the death rate of *S. aureus* is close to 0 in 24 h. Similarly, the TiO_{2PA}_2 μm is also not lethal to *E. coli* in 24 h (Fig. S4b).

4. Discussion

4.1. Characteristic contour for certain pattern vs. bacterial strain

It is noteworthy that the contours of bar charts for *S. aureus* (red curves in Figs. 4b, 5b and 6b) and those for *E. coli* (red curves in Figs. 4d, 5d and 6d) reveal distinct characteristic tendencies in the same motif size range of the same pattern type. This phenomenon may be attributed to the distinct shapes, sizes, and physiological behaviours of the two bacterial strains. Therefore, the characteristic contour corresponding to certain pattern type and bacterial strain deserves to be archived in a database. The database can be used for the surface topography design of medical implants in the future to reduce the infection risk by involving a specific surface topography (certain pattern type + specific motif size) with an antibacterial ability against certain bacterial strains in a real clinical situation.

4.2. Antibacterial mechanism

On the basis of statistical analysis results, the TiO_2 periodic micro/nano-pillar array with sub-micron motif size could effectively inhibit or retard the adhesion, growth, and proliferation of *S. aureus* and *E. coli*. A proposed main antibacterial mechanism of periodic micro/nano-pillar array is illustrated in Fig. 7 and Fig. 8. Briefly, *S. aureus* can adhere (Fig. 7a), elongate & proliferate (Fig. 7b), and colonize (Fig. 7c) on a flat surface as usual, while the bacterial behaviours (Fig. 7d, e, and f) are significantly interfered by the periodic micro/nano-pillar array as evidenced by the compressed shapes of *S. aureus* shown in Fig. 7e and f. Rather than occupying a large area of surface by proliferating to form a close-packed colony (Fig. 7c), the *S. aureus* is imprisoned by a narrow space (Fig. 7f) constructed by the periodic micro/nano-pillar array.

Similarly, both the hypothesis models and the SEM actual observation (Fig. 8a, a′, b, b′, c, and c′) indicate that the elongation and binary fission of *E. coli* are normal when an *E. coli* is on a flat surface. However, when an *E. coli* locates at the bottom of a periodic micro/nano-pillar array, its elongation and binary fission seem to be constrained, as shown in Fig. 8d, d′, e, e′, f, and f′.

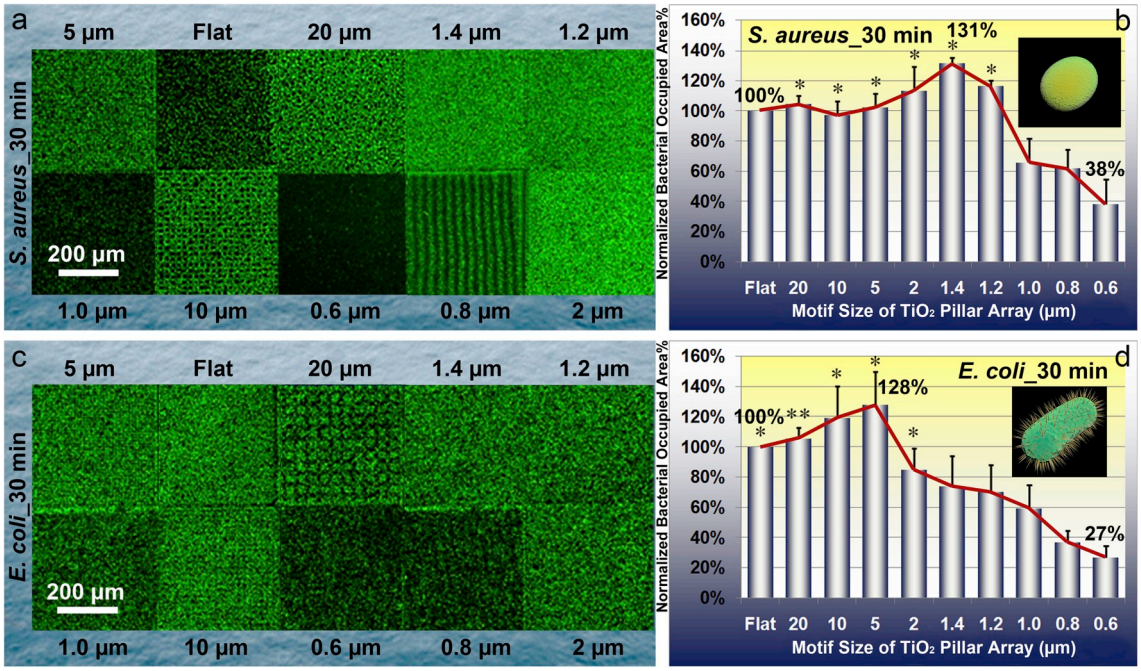

Fig. 4. Characteristics of *S. aureus* and *E. coli* after culturing for 30 min on the TiO_2 periodic micro/nano-pillar arrays. (a) Typical CLSM images of *S. aureus* on one flat area and nine patterned areas, respectively; (b) Quantitative statistical analysis of relative *S. aureus* occupied area percentage which is normalized by that on TiO_2_Flat. Error bar = SEM; (c) Typical CLSM images of *E. coli* on one flat area and nine patterned areas, respectively; (d) Quantitative statistical analysis of relative *E. coli* occupied area percentage which is normalized by that on TiO_2_Flat. Error bar = SEM. One asterisk (*) indicates significant difference at $p < 0.05$, two asterisks (**) indicate significant difference at $p < 0.01$ in t-tests.

It is believed that one main reason for the antibacterial property of periodic micro/nano-pillar array is a spatial confinement size-effect which traps bacteria between pillars, limits the attachment area for bacteria, and impedes the bacterial cell-cell interactions [26,35]. Nevertheless, the antibacterial property cannot be attributed to the photocatalytic effect of TiO_2 since the bacteria were cultured with the samples in the dark.

In addition, the wettability of nine TiO_2 patterned surfaces and one TiO_2 flat surface was systematically investigated since different wettability might result in different affinity for bacteria. Specifically, the

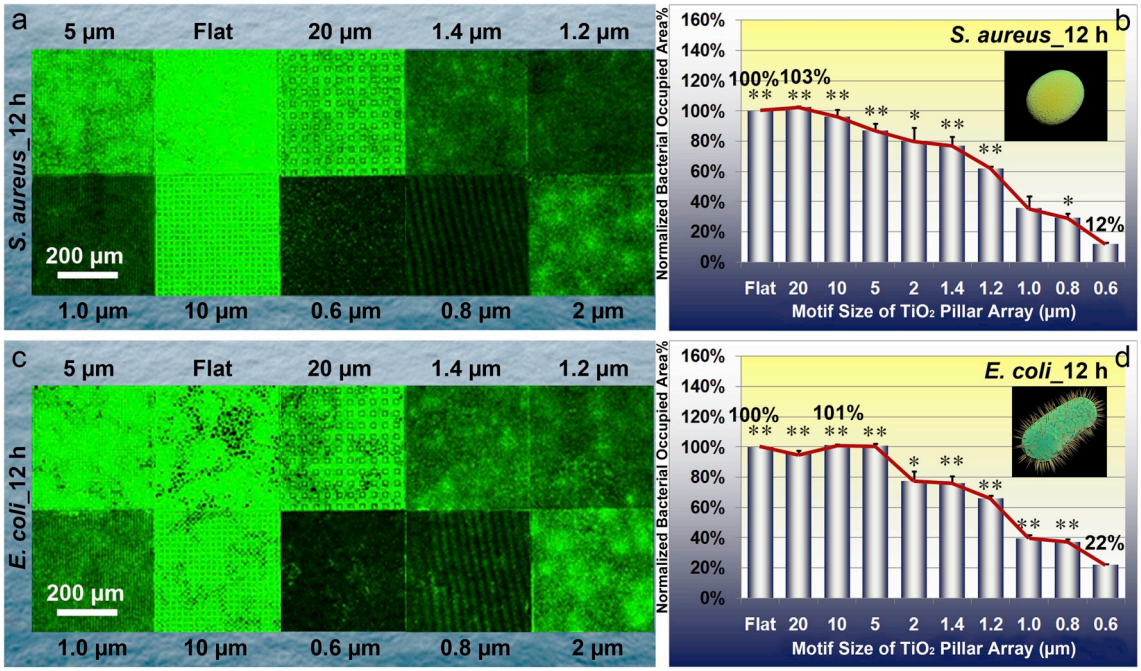

Fig. 5. Characteristics of *S. aureus* and *E. coli* after culturing for 12 h on the TiO_2 periodic micro/nano-pillar arrays. (a) Typical CLSM images of *S. aureus* on one flat area and nine patterned areas, respectively; (b) Quantitative statistical analysis of relative *S. aureus* occupied area percentage which is normalized by that on TiO_2_Flat. Error bar = SEM; (c) Typical CLSM images of *E. coli* on one flat area and nine patterned areas, respectively; (d) Quantitative statistical analysis of relative *E. coli* occupied area percentage which is normalized by that on TiO_2_Flat. Error bar = SEM. One asterisk (*) indicates significant difference at $p < 0.05$, two asterisks (**) indicate significant difference at $p < 0.01$ in t-tests.

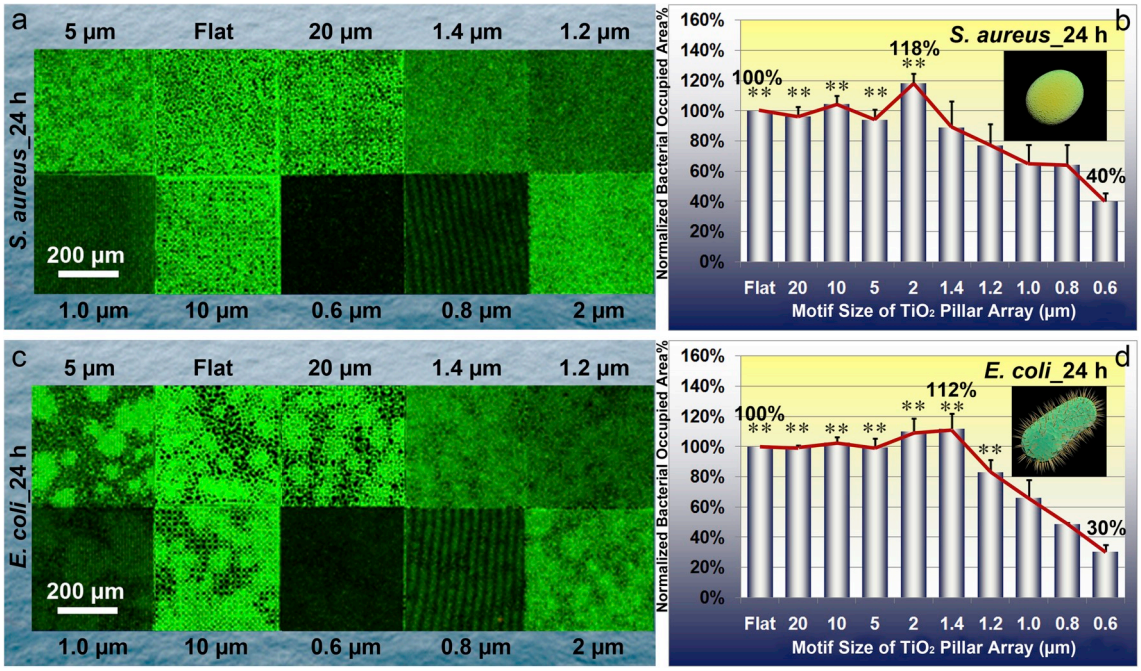

Fig. 6. Characteristics of *S. aureus* and *E. coli* after culturing for 24 h on the TiO_2 periodic micro/nano-pillar arrays. (a) Typical CLSM images of *S. aureus* on one flat area and nine patterned areas, respectively; (b) Quantitative statistical analysis of relative *S. aureus* occupied area percentage which is normalized by that on TiO_2_Flat. Error bar = SEM; (c) Typical CLSM images of *E. coli* on one flat area and nine patterned areas, respectively; (d) Quantitative statistical analysis of relative *E. coli* occupied area percentage which is normalized by that on TiO_2_Flat. Error bar = SEM. One asterisk (*) indicates significant difference at $p < 0.05$, two asterisks (**) indicate significant difference at $p < 0.01$ in t-tests.

pillar array motif size plays a vital role in the wettability of patterned TiO_2 surfaces, since the WCAs monotonically reduce with decreasing the pillar array motif size, as depicted in Fig. 3j. All the ten areas are hydrophilic because their WCAs are smaller than 90° (even smaller than 60°). Among them, the TiO_2_Flat has the largest WCA as 56.4°, while the TiO_{2PA}_0.6 μm possesses the smallest WCA as 16.1°. It is generally believed that super-hydrophobic surfaces have an effective ability in decreasing bacterial adhesion [67,68]. However, in this work, the experimental results (Figs. 4–6) revealed that the TiO_{2PA}_0.6 μm with the smallest WCA (super-hydrophilic) possesses the greatest ability to resist bacterial adhesion. This controversy will not be a surprise. Xu et al. [69] reported that a hydrophilic polyurethane pillar array with a submicron motif size has a higher resistance to bacterial adhesion compared with a flat surface or micron-sized patterns. The reductions in bacterial adhesion are dependent on the pattern motif size which determines the contact area availability for bacteria [69]. Notably, the contact area availability is a principal decisive factor affecting bacterial adhesion on hydrophilic patterned surfaces [69], which could also be used to perfectly explain the experimental results presented in this study.

Generally, the interactions between bacteria and material surfaces can be affected by various properties of the material surface, including wettability, surface energy, charge, chemical components, elastic modulus, topography, and so on [67]. Bacterial behaviours on the material surface could be synergistically influenced by these properties, hardly manipulated by any single property unless it is dominant. This is why mild hydrophobic surfaces cannot always decrease bacterial adhesion [67]. Thus, the spatial confinement size-effect and the limited

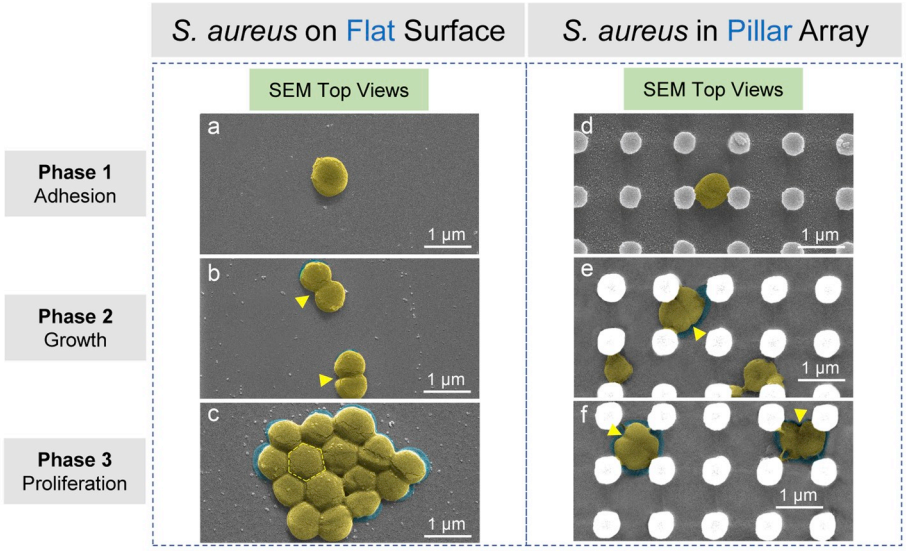

Fig. 7. Antibacterial mechanism of periodic micro/nano-pillar array (*S. aureus*). *S. aureus* on a flat surface: (a) (b) (c) SEM top views (with false color) corresponding to bacteria at Phase 1, 2, and 3. The arrows in (b) indicate binary fission positions. The hexagon in (c) illustrates the shape of a bacterium in the middle of a close-packed bacterial colony. *S. aureus* in a pillar array: (d) (e) (f) SEM top views (with false color) corresponding to bacteria at Phase 1, 2, and 3. The arrows in (e) and (f) indicate binary fission positions. SEM actual observation proves that the pillar array could inhibit the normal elongation & binary fission (e) and colonization (f) of *S. aureus*.

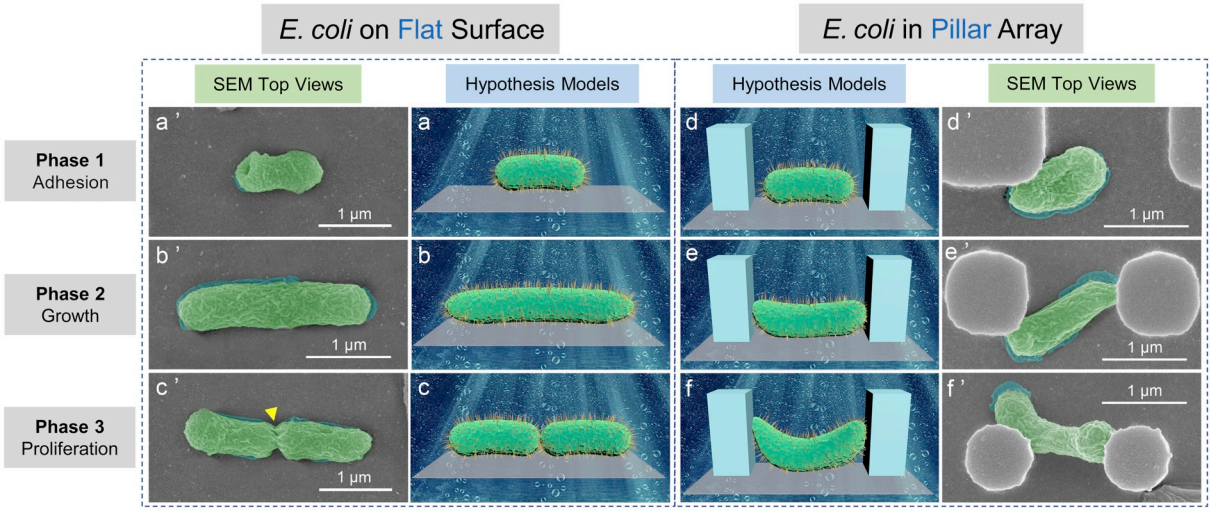

Fig. 8. Antibacterial mechanism of periodic micro/nano-pillar array (*E. coli*). *E. coli* on a flat surface: (a) (b) (c) Hypothesis models corresponding to a bacterium at Phase 1, 2, and 3; (a') (b') (c') SEM top views (with false color) corresponding to a bacterium at Phase 1, 2, and 3. The arrow in (c') indicates a binary fission position. *E. coli* in a pillar array: (d) (e) (f) Hypothesis models corresponding to a bacterium at Phase 1, 2, and 3; (d') (e') (f') SEM top views (with false color) corresponding to a bacterium at Phase 1, 2, and 3. SEM actual observation proves that the pillar array could inhibit the normal elongation (e') and binary fission (f') of *E. coli* as predicted by the hypothesis models in (e) and (f), respectively.

contact area availability are the main antibacterial mechanisms for the hydrophilic TiO_2 periodic micro/nano-pillar array with sub-micron motif size.

5. Conclusions

Here, we designed a novel model substrate which was a combination of periodic micro/nano-pillar array and TiO_2 for basically understanding the topographical bacteriostatic effects of periodic micro/nano-pillar array and the photocatalytic bactericidal activity of TiO_2. Such innovation may potentially exert the synergistic effects by integrating the persistent topographical antibacterial activity and the non-invasive X-ray induced photocatalytic antibacterial property of TiO_2 to combat against antibiotic-resistant implant-associated infections. This work systematically studied how TiO_2 periodic micro/nano-pillar array affected the bacterial behaviours, including bacterial adhesion, growth, proliferation, and viability. The TiO_2 periodic micro/nano-pillar array with sub-micron motif size can significantly inhibit the adhesion, growth, and proliferation of *S. aureus* and *E. coli*. Specifically, TiO_{2PA}_0.6 μm can reduce 62% of *S. aureus* adhesion at 30 min, 73% of *E. coli* adhesion at 30 min, 60% of *S. aureus* colonization at 24 h, and 70% of *E. coli* colonization at 24 h compared with the TiO_2 flat surface. Such antibacterial ability is mainly attributed to a spatial confinement size-effect and limited contact area availability generated by the special topography of TiO_2 periodic micro/nano-pillar array, but cannot be ascribed to the photocatalytic effect of TiO_2 since the bacteria were cultured with the samples in the dark. Rather than using a model material as Si, this study employed a common biocompatible and bioactive biomaterial (TiO_2) to further confirm that the topographical antibacterial effects are independent of substrate chemistry. Moreover, the TiO_2 periodic micro/nano-pillar array is not lethal to *S. aureus* and *E. coli* in 24 h, no matter what the pillar array motif size is (from 20 μm to 0.6 μm). Then, the X-ray induced photocatalytic antibacterial property of TiO_2 periodic micro/nano-pillar array *in vitro* and *in vivo* will be systematically studied in a future work.

Nevertheless, the multi-step fabrication process of the model substrate is somewhat laborious. Besides, the bulk material of the model substrate is still Si instead of Ti of which strength is high enough for clinical applications. Additionally, the photolithography plus magnetron sputtering may not adapt well to a more complicated 3D substrate other than flat surface. Although the model substrate is still far from clinical applications owing to the above-mentioned shortcomings, this study could shed light on the direction of surface topography design for future medical implants to combat against antibiotic-resistant implant-associated infections without using antibiotics, which may eliminate health concerns caused by the widespread, long-term, and excessive usage of antibiotics.

Author contributions

X.G. and Y.L. conceived the experimental system and analyzed the figures and data; X.G. carried out the material synthesis and characterization; and Y.D. performed part of material synthesis and characterization. All authors contributed to the manuscript preparation and revision.

Data and materials availability

All data needed to evaluate the conclusions in the paper are present in the paper. Additional data related to this paper may be requested from the authors.

Conflict of interest

The authors declare no conflict of interest.

Acknowledgements

This work was financially supported by the Natural Science Foundation of Tianjin (General Program, No. 18JCYBJC19500), the Independent Innovation Fund of Tianjin University (No. 2019XZS-0014), and the Research Grants Council of Hong Kong (No. HKUST615408).

Appendix A. Supplementary data

Supplementary data to this article can be found online at https://doi.org/10.1016/j.bioactmat.2019.10.006.

References

[1] L. Montanaro, P. Speziale, D. Campoccia, S. Ravaioli, I. Cangini, G. Pietrocola,

S. Giannini, C.R. Arciola, Scenery of Staphylococcus implant infections in orthopedics, Future Microbiol. 6 (11) (2011) 1329–1349.
[2] C.R. Arciola, D. Campoccia, G.D. Ehrlich, L. Montanaro, Biofilm-based implant infections in orthopaedics, in: G. Donelli (Ed.), Biofilm-Based Healthcare-Associated Infections, Vol I, vol 830, 2015, pp. 29–46.
[3] C.R. Arciola, D. Campoccia, L. Montanaro, Implant infections: adhesion, biofilm formation and immune evasion, Nat. Rev. Microbiol. 16 (7) (2018) 397–409.
[4] S.S. Magill, J.R. Edwards, W. Bamberg, Z.G. Beldavs, G. Dumyati, M.A. Kainer, R. Lynfield, M. Maloney, L. McAllister-Hollod, J. Nadle, S.M. Ray, D.L. Thompson, L.E. Wilson, S.K. Fridkin, multistate point- prevalence survey of health care- associated infections, N. Engl. J. Med. 370 (13) (2014) 1198–1208.
[5] A. Tripathy, P. Sen, B. Su, W.H. Briscoe, Natural and bioinspired nanostructured bactericidal surfaces, Adv. Colloid Interface Sci. 248 (2017) 85–104.
[6] M. Ma, X. Liu, L. Tan, Z. Cui, X. Yang, Y. Liang, Z. Li, Y. Zheng, K.W.K. Yeung, S. Wu, Enhancing the antibacterial efficacy of low-dose gentamicin with 5 minute assistance of photothermy at 50 °C, Biomater. Sci. 7 (4) (2019) 1437–1447.
[7] A.G. Gristina, J. Kolkin, Total joint replacement and sepsis, J. Bone Joint Surg. - Ser. A 65 (1) (1983) 128–134.
[8] Y.H. An, R.J. Friedman, Prevention of sepsis in total joint arthroplasty, J. Hosp. Infect. 33 (2) (1996) 93–108.
[9] Y.H. An, R.J. Friedman, Laboratory methods for studies of bacterial adhesion, J. Microbiol. Methods 30 (2) (1997) 141–152.
[10] W. Zimmerli, A.F. Widmer, M. Blatter, R. Frei, P.E. Ochsner, Role of rifampin for treatment of orthopedic implant-related staphylococcal infections: a randomized controlled trial, J. Am. Med. Assoc. 279 (19) (1998) 1537–1541.
[11] R.O. Darouiche, Treatment of infections associated with surgical implants, N. Engl. J. Med. 350 (14) (2004) 1422–1429.
[12] X. Ge, Antimicrobial biomaterials with non-antibiotic strategy, Biosurf. Biotribol. 5 (3) (2019) 71–82.
[13] Q. Wang, P. Tang, X. Ge, P. Li, C. Lv, M. Wang, K. Wang, L. Fang, X. Lu, Experimental and simulation studies of strontium/zinc-codoped hydroxyapatite porous scaffolds with excellent osteoinductivity and antibacterial activity, Appl. Surf. Sci. 462 (2018) 118–126.
[14] Q. Wang, P. Li, P. Tang, X. Ge, F. Ren, C. Zhao, J. Fang, K. Wang, L. Fang, Y. Li, C. Bao, X. Lu, K. Duan, Experimental and simulation studies of strontium/fluoride-codoped hydroxyapatite nanoparticles with osteogenic and antibacterial activities, Colloid Surf. B-Biointerfaces 182 (2019) 110359.
[15] P. Li, Z. Jia, Q. Wang, P. Tang, M. Wang, K. Wang, J. Fang, C. Zhao, F. Ren, X. Ge, X. Lu, A resilient and flexible chitosan/silk cryogel incorporated Ag/Sr co-doped nanoscale hydroxyapatite for osteoinductivity and antibacterial properties, J. Mater. Chem. B 6 (45) (2018) 7427–7438.
[16] D. Gan, T. Xu, W. Xing, X. Ge, L. Fang, K. Wang, F. Ren, X. Lu, Mussel-inspired contact-active antibacterial hydrogel with high cell affinity, toughness, and recoverability, Adv. Funct. Mater. 29 (1) (2019) 1805964.
[17] Q. Du, D. Wei, Y. Wang, S. Cheng, S. Liu, Y. Zhou, D. Jia, The effect of applied voltages on the structure, apatite-inducing ability and antibacterial ability of micro arc oxidation coating formed on titanium surface, Bioact. Mater. 3 (4) (2018) 426–433.
[18] J. Qiu, L. Liu, H. Zhu, X. Liu, Combination types between graphene oxide and substrate affect the antibacterial activity, Bioact. Mater. 3 (3) (2018) 341–346.
[19] A. Mohandas, S. Deepthi, R. Biswas, R. Jayakumar, Chitosan based metallic nanocomposite scaffolds as antimicrobial wound dressings, Bioact. Mater. 3 (3) (2018) 267–277.
[20] M. Li, P. Xiong, F. Yan, S. Li, C. Ren, Z. Yin, A. Li, H. Li, X. Ji, Y. Zheng, Y. Cheng, An overview of graphene-based hydroxyapatite composites for orthopedic applications, Bioact. Mater. 3 (1) (2018) 1–18.
[21] J. Hasan, K. Chatterjee, Recent advances in engineering topography mediated antibacterial surfaces, Nanoscale 7 (38) (2015) 15568–15575.
[22] D.P. Linklater, S. Juodkazis, E.P. Ivanova, Nanofabrication of mechano-bactericidal surfaces, Nanoscale 9 (43) (2017) 16564–16585.
[23] Y. Luan, S. Liu, M. Pihl, H.C. van der Mei, J. Liu, F. Hizal, C.-H. Choi, H. Chen, Y. Ren, H.J. Busscher, Bacterial interactions with nanostructured surfaces, Curr. Opin. Colloid Interface Sci. 38 (2018) 170–189.
[24] A. Elbourne, J. Chapman, A. Gelmi, D. Cozzolino, R.J. Crawford, V.K. Truong, Bacterial-nanostructure interactions: the role of cell elasticity and adhesion forces, J. Colloid Interface Sci. 546 (2019) 192–210.
[25] J. Sun, B. Bhushan, Nanomanufacturing of bioinspired surfaces, Tribol. Int. 129 (2019) 67–74.
[26] M. Yang, Y. Ding, X. Ge, Y. Leng, Control of bacterial adhesion and growth on honeycomb-like patterned surfaces, Colloid Surf. B-Biointerfaces 135 (2015) 549–555.
[27] E.W. McAllister, L.C. Carey, P.G. Brady, R. Heller, S.G. Kovacs, The role of polymeric surface smoothness of biliary stents in bacterial adherence, biofilm deposition, and stent occlusion, Gastrointest. Endosc. 39 (3) (1993) 422–425.
[28] M. Quirynen, H.C. van der Mei, C.M. Bollen, A. Schotte, M. Marechal, G.I. Doornbusch, I. Naert, H.J. Busscher, D. van Steenberghe, An in vivo study of the influence of the surface roughness of implants on the microbiology of supra- and subgingival plaque, J. Dent. Res. 72 (9) (1993) 1304–1309.
[29] Y.H. An, R.J. Friedman, R.A. Draughn, E.A. Smith, J.H. Nicholson, J.F. John, Rapid quantification of staphylococci adhered to titanium surfaces using image analyzed epifluorescence microscopy, J. Microbiol. Methods 24 (1) (1995) 29–40.
[30] R.L. Taylor, J. Verran, G.C. Lees, A.J.P. Ward, The influence of substratum topography on bacterial adhesion to polymethyl methacrylate, J. Mater. Sci. Mater. Med. 9 (1) (1998) 17–22.
[31] H. Tang, T. Cao, X. Liang, A. Wang, S.O. Salley, J. McAllister Ii, K.Y.S. Ng, Influence of silicone surface roughness and hydrophobicity on adhesion and colonization of Staphylococcus epidermidis, J. Biomed. Mater. Res. A 88 (2) (2009) 454–463.
[32] M.J. Dalby, N. Gadegaard, R. Tare, A. Andar, M.O. Riehle, P. Herzyk, C.D.W. Wilkinson, R.O.C. Oreffo, The control of human mesenchymal cell differentiation using nanoscale symmetry and disorder, Nat. Mater. 6 (12) (2007) 997–1003.
[33] C.M. Magin, S.P. Cooper, A.B. Brennan, Non-toxic antifouling strategies, Mater. Today 13 (4) (2010) 36–44.
[34] X. Ge, Topographical effects on bacterial behaviors, Doctor of Philosophy, Department of Mechanical Engineering, The Hong Kong University of Science and Technology, Hong Kong, 2011.
[35] X. Ge, Y. Leng, X. Lu, F. Ren, K. Wang, Y. Ding, M. Yang, Bacterial responses to periodic micropillar array, J. Biomed. Mater. Res. A 103 (1) (2015) 384–396.
[36] E.P. Ivanova, J. Hasan, H.K. Webb, V.K. Truong, G.S. Watson, J.A. Watson, V.A. Baulin, S. Pogodin, J.Y. Wang, M.J. Tobin, C. Löbbe, R.J. Crawford, Natural bactericidal surfaces: mechanical rupture of pseudomonas aeruginosa cells by cicada wings, Small 8 (16) (2012) 2489–2494.
[37] J. Hasan, H.K. Webb, T. Vi Khanh, S. Pogodin, V.A. Baulin, G.S. Watson, J.A. Watson, R.J. Crawford, E.P. Ivanova, Selective bactericidal activity of nanopatterned superhydrophobic cicada Psaltoda claripennis wing surfaces, Appl. Microbiol. Biotechnol. 97 (20) (2013) 9257–9262.
[38] K. Nowlin, A. Boseman, A. Covell, D. LaJeunesse, Adhesion-dependent rupturing of Saccharomyces cerevisiae on biological antimicrobial nanostructured surfaces, J. R. Soc. Interface 12 (102) (2015) 20140999.
[39] S.M. Kelleher, O. Habimana, J. Lawler, B. O'Reilly, S. Daniels, E. Casey, A. Cowley, Cicada wing surface topography: an investigation into the bactericidal properties of nanostructural features, ACS Appl. Mater. Interfaces 8 (24) (2016) 14966–14974.
[40] H. Shahali, J. Hasan, A. Mathews, H. Wang, C. Yan, T. Tesfamichael, P.K.D.V. Yarlagadda, Multi-biofunctional properties of three species of cicada wings and biomimetic fabrication of nanopatterned titanium pillars, J. Mater. Chem. B 7 (8) (2019) 1300–1310.
[41] J. Ye, J. Deng, Y. Chen, T. Yang, Y. Zhu, C. Wu, T. Wu, J. Jia, X. Cheng, X. Wang, Cicada and catkin inspired dual biomimetic antibacterial structure for the surface modification of implant material, Biomater. Sci. 7 (7) (2019) 2826–2832.
[42] E.P. Ivanova, J. Hasan, H.K. Webb, G. Gervinskas, S. Juodkazis, V.K. Truong, A.H.F. Wu, R.N. Lamb, V.A. Baulin, G.S. Watson, J.A. Watson, D.E. Mainwaring, R.J. Crawford, Bactericidal activity of black silicon, Nat. Commun. 4 (2013) 2838.
[43] G.S. Watson, D.W. Green, L. Schwarzkopf, X. Li, B.W. Cribb, S. Myhra, J.A. Watson, A gecko skin micro/nano structure - a low adhesion, superhydrophobic, anti-wetting, self-cleaning, biocompatible, antibacterial surface, Acta Biomater. 21 (2015) 109–122.
[44] C.R. Arciola, Y.H. An, D. Campoccia, M.E. Donati, L. Montanaro, Etiology of implant orthopedic infections: a survey on 1027 clinical isolates, Int. J. Artif. Organs 28 (11) (2005) 1091–1100.
[45] R. Brayner, R. Ferrari-Iliou, N. Brivois, S. Djediat, M.F. Benedetti, F. Fievet, Toxicological impact studies based on Escherichia coli bacteria in ultrafine ZnO nanoparticles colloidal medium, Nano Lett. 6 (4) (2006) 866–870.
[46] X. Wang, F. Yang, W. Yang, X. Yang, A study on the antibacterial activity of one-dimensional ZnO nanowire arrays: effects of the orientation and plane surface, Chem. Commun. (42) (2007) 4419–4421.
[47] X. Wang, H. Zhu, F. Yang, X. Yang, Biofilm-engineered nanostructures, Adv. Mater. 21 (27) (2009) 2815–2818.
[48] F. Yu, X. Fang, H. Jia, M. Liu, X. Shi, C. Xue, T. Chen, Z. Wei, F. Fang, H. Zhu, H. Xin, J. Feng, X. Wang, Zn or O? An atomic level comparison on antibacterial activities of zinc oxides, Chem.-Eur. J. 22 (24) (2016) 8053–8058.
[49] Q. Li, S. Mahendra, D.Y. Lyon, L. Brunet, M.V. Liga, D. Li, P.J.J. Alvarez, Antimicrobial nanomaterials for water disinfection and microbial control: potential applications and implications, Water Res. 42 (18) (2008) 4591–4602.
[50] A.B. Djurisic, X. Chen, Y.H. Leung, A.M.C. Ng, ZnO nanostructures: growth, properties and applications, J. Mater. Chem. 22 (14) (2012) 6526–6535.
[51] L.H. Li, Y.M. Kong, H.W. Kim, Y.W. Kim, H.E. Kim, S.J. Heo, J.Y. Koak, Improved biological performance of Ti implants due to surface modification by micro-arc oxidation, Biomaterials 25 (14) (2004) 2867–2875.
[52] F. Lindberg, J. Heinrichs, F. Ericson, P. Thomsen, H. Engqvist, Hydroxylapatite growth on single-crystal rutile substrates, Biomaterials 29 (23) (2008) 3317–3323.
[53] X. Lu, H. Zhang, Y. Guo, Y. Wang, X. Ge, Y. Leng, F. Watari, Hexagonal hydroxyapatite formation on TiO2 nanotubes under urea modulation, CrystEngComm 13 (11) (2011) 3741–3749.
[54] H.-K. Tsou, P.-Y. Hsieh, M.-H. Chi, C.-J. Chung, J.-L. He, Improved osteoblast compatibility of medical-grade polyetheretherketone using arc ionplated rutile/anatase titanium dioxide films for spinal implants, J. Biomed. Mater. Res. A 100A (10) (2012) 2787–2792.
[55] K.P. Kuhn, I.F. Chaberny, K. Massholder, M. Stickler, V.W. Benz, H.G. Sonntag, L. Erdinger, Disinfection of surfaces by photocatalytic oxidation with titanium dioxide and UVA light, Chemosphere 53 (1) (2003) 71–77.
[56] H.A. Foster, I.B. Ditta, S. Varghese, A. Steele, Photocatalytic disinfection using titanium dioxide: spectrum and mechanism of antimicrobial activity, Appl. Microbiol. Biotechnol. 90 (6) (2011) 1847–1868.
[57] F. Schmidt-Stein, R. Hahn, J.F. Gnichwitz, Y.Y. Song, N.K. Shrestha, A. Hirsch, P. Schmuki, X-ray induced photocatalysis on TiO_2 and TiO_2 nanotubes: degradation of organics and drug release, Electrochem. Commun. 11 (11) (2009) 2077–2080.
[58] Y. Ding, Y. Leng, N. Huang, P. Yang, X. Lu, X. Ge, F. Ren, K. Wang, L. Lei, X. Guo, Effects of microtopographic patterns on platelet adhesion and activation on titanium oxide surfaces, J. Biomed. Mater. Res. A 101A (3) (2013) 622–632.
[59] X. Ge, C. Ren, X. Lu, Z. Li, G. Chen, K. Wang, F. Ren, Q. Wang, M. Wang, X. An, B. Qian, Surfactant-free electrochemical synthesis of fluoridated hydroxyapatite nanorods for biomedical applications, Ceram. Int. 45 (14) (2019) 17336–17343.

[60] L. Zhou, X. Ge, C. Ren, G. Chen, In-situ high temperature XRD and TEM study of the thermal stability and sintering behavior of octacalcium phosphate, J. Alloy. Compd. 778 (2019) 72–76.
[61] X. Ge, F. Ren, Y. Leng, Electrochemical deposition of fluoridated calcium phosphate thin film on titanium substrates, Adv. Mater. Res. 47–50 (2008) 1387–1390.
[62] X. Ge, Y. Leng, C. Bao, S.L. Xu, R. Wang, F. Ren, Antibacterial coatings of fluoridated hydroxyapatite for percutaneous implants, J. Biomed. Mater. Res. A 95 A (2) (2010) 588–599.
[63] X. Ge, Y. Leng, F. Ren, X. Lu, Integrity and zeta potential of fluoridated hydroxyapatite nanothick coatings for biomedical applications, J. Mech. Behav. Biomed. Mater. 4 (7) (2011) 1046–1056.
[64] K. Wang, Y. Leng, X. Lu, F. Ren, X. Ge, Y. Ding, Theoretical analysis of protein effects on calcium phosphate precipitation in simulated body fluid, CrystEngComm 14 (18) (2012) 5870–5878.
[65] X. Lu, Y. Leng, Quantitative analysis of osteoblast behavior on microgrooved hydroxyapatite and titanium substrata, J. Biomed. Mater. Res. A 66 (3) (2003) 677–687.
[66] X. Lu, Y. Leng, Comparison of the osteoblast and myoblast behavior on hydroxyapatite microgrooves, J. Biomed. Mater. Res. B Appl. Biomater. 90B (1) (2009) 438–445.
[67] X. Zhang, L. Wang, E. Levanen, Superhydrophobic surfaces for the reduction of bacterial adhesion, RSC Adv. 3 (30) (2013) 12003–12020.
[68] Y. Lai, J. Huang, Z. Cui, M. Ge, K.-Q. Zhang, Z. Chen, L. Chi, Recent advances in TiO2-based nanostructured surfaces with controllable wettability and adhesion, Small 12 (16) (2016) 2203–2224.
[69] L.-C. Xu, C.A. Siedlecki, Staphylococcus epidermidis adhesion on hydrophobic and hydrophilic textured biomaterial surfaces, Biomed. Mater. 9 (3) (2014) 035003.